# RSC Advances

**ROYAL SOCIETY OF CHEMISTRY**

www.rsc.org/advances

# RSC Advances

## ARTICLE

# Competitive Lithium and Sodium Intercalation into Sodium Manganese Phospho-Olivine NaMnPO$_4$ Covered with Carbon Black

T. Boyadzhieva,[a] V. Koleva,[a] E. Zhecheva,[a] D. Nihtianova,[a,b] L. Mihaylov[c] and R. Stoyanova[a*]

In this contribution we provide novel data on the reversible lithium and sodium ions intercalation into a sodium-manganese phospho-olivine NaMnPO$_4$, when it is used as a cathode in model lithium-ion cells. The ion-exchange reaction involving the participation of KMnPO$_4$.H$_2$O dittmarite as precursor was chosen for the preparation of NaMnPO$_4$. The NaMnPO$_4$ particles were covered with carbonaceous materials to improve the electrical conductivity and electrolyte wetting. The procedure includes ball-milling of NaMnPO$_4$ with conductive carbon black additives Super C/65, followed by thermal treatment. The mechanically treated samples consist of well crystallized phospho-olivine phase NaMnPO$_4$ free of any anti-site defects and disordered carbon species with graphite like medium-range order. The composite NaMnPO$_4$/C material manifests a reversible capacity between 80-85 mAh/g in model lithium cells versus lithium anode. Prior to the electrochemical test, the chemical inertness of NaMnPO$_4$ in the lithium electrolyte is studied by soaking phospho-olivines in the solution of LiPF$_6$ in EC:DMC. The mechanism of the reversible intercalation/deintercalation cycling is investigated using *ex-situ* X-ray powder diffraction, TEM and high-angle annular dark field STEM analysis, infrared spectroscopy and electron paramagnetic resonance spectroscopy (EPR). The study demonstrates, for the first time, that NaMnPO$_4$ is able to intercalate reversibly both Na$^+$ and Li$^+$ ions following the chemical reaction Li$_x$Na$_{1-x}$MnPO$_4$ $\leftrightarrow$ Li$_{0.0}$Na$_{0.5}$MnPO$_4$ (0.25≤x≤0.45).

## Introduction

Lithium-transition metal phosphates with olivine type of structure, LiMPO$_4$ (M = Mn, Fe, Co and Ni), have attracted significant research interest as cathodic materials for high-power lithium ion batteries with potential to power electric vehicles.[1,2] Among them, LiFePO$_4$ displays the best electrochemical performance in view of higher rate capability and better cycling stability.[1,2] In comparison with LiFePO$_4$, the LiMnPO$_4$ appears to be more promising since it offers a higher potential of Li$^+$ intercalation (4.1 V versus 3.45 V, respectively), as a result of which a higher theoretical energy density can be achieved for LiMnPO$_4$ (701 Wh/kg versus 586 Wh/kg).[3] However, LiMnPO$_4$ displays a limited rate capability due to its lower electronic conductivity (10$^{-10}$ – 10$^{-14}$ S cm$^{-1}$ versus 10$^{-9}$ S cm$^{-1}$) and greater lattice distortion due to the Jahn-Teller's instability of Mn$^{3+}$ ions.[4,5] All these factors, together with an anisotropic Li diffusion, determine the critical dependence of the electrochemical properties of LiMnPO$_4$ on the method of synthesis.[6] Two main types of synthetic procedures have been

developed during the last years.[6-8] The first one aims at improving the total electrical conductivity by coating the phospho-olivines with more conductive layers (such as carbon),[6,7] the second type of procedure is directed towards designing the morphology of phospho-olivines in order to make the Li diffusion more easy.[6,8]

Recently we have demonstrated that sodium compounds, instead of their Li analogues, can be used directly as cathodes in lithium ion batteries.[9-11] This is a consequence of the ability of sodium compounds to participate in ion-exchange reactions between Na$^+$ and Li$^+$ ions. As a result, the *in-situ* generated lithium compounds exhibit different electrochemical properties in comparison with those obtained prior to their use in electrochemical cells.[12] The direct use of sodium-containing compounds as electrode materials in lithium ion batteries is beneficial especially in the case of layered oxides on the basis of vanadium, titanium and manganese such as Na$_x$V$_3$O$_8$, Na$_{2/3}$Mn$_{1-x}$Fe$_x$O$_2$, $\alpha$-Na$_{0.66}$MnO$_{2.13}$, sodium titanate.[13-16] Concerning polyanion-based compounds, it has been demonstrated that the lithium intercalated jarosite hydroxysulfate Li$_{2+x}$NaFe$_3$(SO$_4$)$_2$(OH)$_6$ (with 0<x<0.5) exhibits reversible electrochemical lithium intercalation/de-intercalation through a solid solution-like process, leading back to the oxidized jarosite Li$_x$NaFe$_3$(SO$_4$)$_2$(OH)$_6$ (with 0.3<x<0.6), with redox cycling at 2.82V and a capacity of 110 mAh/g at C/20.[17] To the best of our knowledge this concept has not yet

[a.] *Institute of General and Inorganic Chemistry, Bulgarian Academy of Sciences 1113 Sofia, Bulgaria.*
[b.] *Institute of Mineralogy and Crystallography, Bulgarian Academy of Sciences, 1113 Sofia, Bulgaria.*
[c.] *Faculty of Chemistry and Pharmacy, Sofia University, 1164 Sofia, Bulgaria.*
* e-mail: radstoy@svr.igic.bas.bg
See DOI: 10.1039/x0xx00000x

been examined in the case of manganese-based phospho-olivines.

In comparison with LiMnPO$_4$, NaMnPO$_4$ posses two structure modifications: maricite-type and olivine-type of structure.[18,19] Although both structural modifications display the same framework composed of phosphate groups (space group *Pnma*), the occupancy of M1(*4a*) and M2(*4c*) positions by Na$^+$ and Mn$^{2+}$ ions is different: for the olivine-type of structure, Na$^+$ and Mn$^{2+}$ occupy preferentially M1 and M2 sites, while the opposite occupancy is observed in the maricite-type of structure. In the olivine structure, Na$^+$-containing octahedra share edges and form *zig-zag* chains along the *b* axis.[18] This is the preferred direction of more favorable diffusion of alkaline ions through the olivine crystal structure.[20,5] The maricite structure is electrochemically inactive since the Na$^+$ ions mobility is blocked.[21] However, it is the maricite phase that is the thermodynamically stable modification of NaMnPO$_4$.

Based on ion-exchange reaction, we have already reported a facile low-temperature method for the preparation of both Li- and Na-containing phospho-olivines.[22-24] The method is based on the ion exchange reaction by using of KMnPO$_4$.H$_2$O having dittmarite-type of structure as a precursor. The reaction mechanism includes ionic exchange of K$^+$ for Li$^+$ or Na$^+$ in the framework of the dittmarite structure, followed by H$_2$O release and formation of the olivine-type of structure.[22,23] The ionic exchange reaction is a consequence of the structural similarity between the dittmarite and olivine structures. Both structures consist of layers composed of corner-sharing metal octahedra bridged through the oxygen atoms of the PO$_4^{3-}$ groups. The topology of the Mn(2+)-phosphate layer in the *ac* plane of KMnPO$_4$.H$_2$O matches the topology of the Mn(2+)-phosphate layer in the *bc* plane of Li/NaMPO$_4$. As a result, the preferred orientation of the precursor dittmarite crystallites remains the same as in the targeted olivine composition.[22,23] This method is effective for the preparation of the electrochemically active LiMnPO$_4$ compositions.[24]

In this contribution, we provide new data on the reversible intercalation of Na$^+$ and Li$^+$ into NaMnPO$_4$ with an olivine-type of structure. The ion-exchange reaction involving the participation of KMnPO$_4$.H$_2$O dittmarite as precursor was chosen for the preparation of NaMnPO$_4$. The NaMnPO$_4$ particles were covered with carbonaceous materials to improve the electrical conductivity and electrolyte wetting. The procedure includes ball-milling followed by thermal treatment. The crystalline structure and morphology of NaMnPO$_4$/C composite was analyzed by means of X-ray powder diffraction, SEM, SAED and HRTEM, IR and Raman spectroscopy. The intercalation properties of NaMnPO$_4$ were tested in model lithium cells versus lithium anode. Prior to the electrochemical test, the chemical inertness of NaMnPO$_4$ in the lithium electrolyte is studied by soaking phospho-olivines in the solution of LiPF$_6$ in EC:DMC. The structural changes during intercalation/deintercalation cycling are monitored by *ex-situ* X-ray powder diffraction, TEM and high angle annular dark field STEM analysis, IR spectroscopy and EPR.

## Experimental

Sodium manganese phospho-olivine NaMnPO$_4$ was obtained by an ion-exchange reaction using dittmaritte–type KMnPO$_4$.H$_2$O as precursor at 200°C. The details are given elsewhere.[23] Briefly, the dittmarite precursor KMnPO$_4$.H$_2$O was mixed with NaCH$_3$COO.3H$_2$O at a ratio of 1:10. The mixture is heated at 200 $^o$C for 15 hours. After cooling down to room temperature, the product was thoroughly washed with water and ethyl alcohol to remove the unreacted salts, filtered and dried in air for about 5 h. Under these conditions, pure olivine phase of NaMnPO$_4$ was formed. To improve the degree of crystallinity, NaMnPO$_4$ was further annealed at 400 °C for 10 h under argon atmosphere. The composite material was prepared by ball-milling of pristine NaMnPO$_4$ with 15 % conductive carbon black additives Super C65 (TIMCAL) for 4h at a speed of 300 rpm using planetary "Pulverisette 6" mill (Fritsch) with agate balls ($\phi$ 10 mm). The sample to balls ratio was 10:1. The ball-milled composite NaMnPO$_4$/C was thermally treated under argon at 400 °C for 3 h. This sample will be denoted as NMP/C composite, while pristine NMP will be used for the untreated sample.

As a reference sample we used LiMnPO$_4$ obtained by an ion-exchange reaction from the same KMnPO$_4$.H$_2$O precursor. The synthesis procedure was described previously.[22,24] In order to eliminate any anti-site defects, LiMnPO$_4$ was annealed at 500 $^o$C. The composite of LiMnPO$_4$ with carbon additives was also prepared following the above mentioned ball-milling process.

The XRD patterns of pristine NMP and NMP/C composite were registered by using a Bruker Advance 8 diffractometer (CuK$\alpha$ radiation), at 0.02$^o$ 2$\theta$ step of 10 s duration. The structural analysis was made by the Rietveld method with FULLPROF program.[25] The diffractometer point zero, the Lorentzian/Gaussian fraction of the pseudo-Voigt peak function, scale factor, the unit cell parameters (*a , b* and *c*), the thermal factors for the *4a*, *4c* and *8d* positions and the line half-width parameters were refined. The preferred orientation was estimated by the modified March's function with G$_1$ refinable parameter [26]: there is no preferable orientation for G$_1$ = 1 and a preferred orientation with dominant plate-like habit for G$_1$ < 1. The cationic occupancy factors were determined taking into account that the total occupancies of the *4a*, and *4c* metal sites are equal to unity. The crystallite size of NaMnPO$_4$ compositions was calculated by Scherrer's equation: D$_{hkl}$ = $\lambda$ /(($\beta^2$-$\beta_o^2$)$^{1/2}$ cos$\theta_{hkl}$), where $\lambda$(CuK$_\alpha$)=0.15418 nm, $\beta$ is the peak width at the half height corrected with instrumental broadening and $\theta_{hkl}$ is Bragg's angle. The line width was determined by profile analysis using a WinPlotr program.

The morphology of NMP and NMP/C was observed by JEOL JSM-5510 scanning electron microscope. The TEM investigations were performed on a JEOL 2100 transmission electron microscope and a JEOL 2100 XEDS: Oxford Instruments, X-MAX$^N$ 80T CCD Camera ORIUS 1000, 11 Mp, GATAN at accelerating voltage of 200 kV. The specimens were prepared by grinding and dispersing the powders in ethanol by ultrasonic treatment for 6 minutes. The suspensions were dripped on standard holey carbon/Cu grids. The analysis was carried out by the Digital Micrograph software.

The IR spectra of pristine NMP and composites NMP/C were recorded on a Fourier transform Nicolet Avatar-320 instrument (resolution < 2 cm$^{-1}$) using KBr disks. Only the IR spectrum of the

electrolyte was measured in Nujol mull. The Raman spectra were obtained by LabRam 300 (Horiba Jobin-Yvon) micro-Raman spectrometer at room temperature using a He–Ne laser operating at 633 nm.

The oxidation state of Mn ions in NMP/C composites was determined by a Bruker EMX[plus] EPR spectrometer operating in the X-band (9.4 GHz) in the temperature range of 100 – 400 K.

The electrochemical charge-discharge curves of composites NMP/C were examined by using EL-CELL type two-electrode cells comprising Li|LiPF$_6$ (EC:DMC)|NaMnPO$_4$. The positive electrode, supported onto an aluminium foil, was a mixture containing 80% of the active NaMnPO$_4$/C composition, 7.5% C-NERGY KS 6 L graphite (TIMCAL), 7.5% Super C65 (TIMCAL) and 5% polyvinylidene fluoride (PVDF). The loaded mass of active materials on Al collectors was about of 11 mg. The electrolyte was a 1M LiPF$_6$ solution in ethylene carbonate and dimethyl carbonate (1:1 by volume) with less than 20 ppm of water (0.2 ml electrolyte solution was used). The lithium electrodes consisted of a clean lithium metal disk with diameter of 18 mm. The cells were mounted in a dry box under argon atmosphere. The intercalation/deintercalation cycling was carried out using an eight-channel Arbin BT2000 system in galvanostatic mode. The charge and discharge rates were expressed as C/h, where h is the hours needed for the insertion of one lithium per formula unit at the applied current intensity. The model lithium cell was cycled between 4.5 and 2.5 V at C/20 and C/50 rates. The CV test was carried out by using a three electrode cell and PAR Potentiostat/Galvanostat, Model 273A, in the potential window of 1.7–4.7 V and at a scan rate of 0.05 mV/s. The CV curves are recorded after 5 galvanostatic charge/discharge cycles between 2.5 and 4.5 V.

The chemical reactivity of NaMnPO$_4$ with lithium electrolyte was monitored by soaking pristine NMP and composite NMP/C in the solution of LiPF$_6$ salt in EC:DMC for 40 days. All the experiments were carried out in dry box. After the soaking, pristine NMP and composite NMP/C were washed with electrolyte and were dried on pieces of filter paper for 24 h in the dry box. The so treated samples were subjected for XRD and IR spectroscopy measurements. A part of the suspension was also washed with acetone (out of dry box) and the IR spectrum of such a sample was also recorded.

The structural changes of electrode samples during reversible intercalation/deintercalation cycling were analyzed with lithium half-cells stopped at selected potentials. The electrochemical cells were disassembled insight a glove-box, followed by removing and washing of the working electrodes with EC. For the XRD experiments, the electrode samples were covered with parafilm in order to avoid the water contamination. For the TEM experiments, the specimens were dispersed in acetone and the suspensions were dripped on standard holey carbon/Cu grids. For the EPR experiments, the quartz tube was filled with electrodes inside the glove-box.

## Results and discussion

### Structure and morphology of composite NaMnPO$_4$/C

Figure 1 compares the XRD patterns of pristine NMP and NMP/C composite. All diffraction patterns were analyzed within the

framework of the structural model comprising only one phase with olivine-type of structure. It is worth mentioning that no diffraction peaks due to carbon additives were observed, which is consistent with their amorphous state. The lattice parameters of pristine NMP are identical with that for composite NMP/C: $a$ = 10.5177(3) Å, $b$ = 6.3144(2) Å, $c$= 4.9873(2) Å, $V$ = 331.227(22) Å$^3$ for pristine NMP and
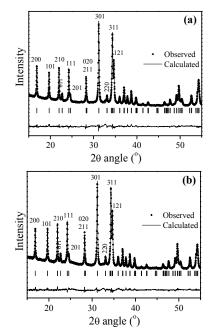


**Figure 1.** Rietveld refinement of the XRD patterns of pristine NaMnPO$_4$ (a) and NaMnPO$_4$/C composite (b).

$a$ = 10.5167(4) Å, $b$ = 6.3163(2) Å, $c$= 4.9885(2) Å, $V$ = 331.378(25) Å$^3$ for NMP/C. On the one hand, these values are in good agreement with those reported previously for NaMnPO$_4$ in the form of single crystal and NaMnPO$_4$ obtained at 200 $^o$C.[23,19] On the other, the identical lattice parameters indicate that the olivine structure remains stable after ball-milling procedure.

Since the olivine modification of NaMnPO$_4$ is thermodynamically unstable, the next issue that should be considered is the possible creation of structural anti-site defects including the exchange of ions between M1 and M2 positions. These kinds of defects have already been observed in LiMnPO$_4$.[27,28] The Rietveld analysis evidences that NMP and NMP/C have an ordered olivine-type of structure, where metal *4a* and *4c* crystallographic sites are entirely occupied by Na and Mn ions, respectively (the refined site occupancy is 1.00 for the two ions). This proves that the ball-milling procedure does not create any defects in the composite material.

The only characteristics that are changed are the XRD peak intensities. The Rietveld's refinement can be interpreted by a preferred orientation of olivine crystallites along the [100] direction: R$_b$=0.039, goodness of fit G$_o$F=1.8 and G1=0.76 for pristine sample and R$_b$=0.048, G$_o$F=1.5 and G1=0.82 for NaMnPO$_4$/C. The observation of preferred orientation coincides with our previous studies on the formation of NaMnPO$_4$ with controlled surface morphology by using template-directed

dittmarite precursors.[23] The important finding here is the comparison of the degree of crystallite orientation: there is a trend of increase in the G1-parameter together with decrease in $G_oF$ for NMP/C. This means that ball-milling procedure reduces the degree of preferred crystallite orientation in the NaMnPO$_4$/C composite. The line-width increases only slightly after ball-milling: the line broadening corresponds to a slight reduction in crystallites sizes from 60 nm in pristine NaMnPO$_4$ to 55 nm in NaMnPO$_4$/C composite.

The stability of the NaMnPO$_4$ olivine structure is further supported by the IR spectra of the pristine and ball-milled samples (Fig. 2). Both NMP and NMP/C samples display the typical IR bands for the PO$_4^{3-}$ groups in the olivine-type of structure: five bands at 943 sh/969/1060/1078/1129 cm$^{-1}$ due to the PO$_4$ stretching vibrations ($\nu_1$ and $\nu_3$ modes) and the bands at 630sh/618/580/545 cm$^{-1}$ originate from the PO$_4$ bending vibrations ($\nu_4$ modes) (Fig. 2). The two IR spectra are identical within the experimental resolution
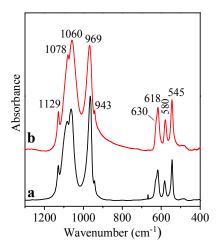


**Figure 2.** IR spectra of pristine NMP (a) and NMP/C composite (b).

(up to 2 cm$^{-1}$), thus indicating that the local structure of the phosphate groups in NaMnPO$_4$/C olivine phase remains unchanged after the ball-milling.

The presence of carbon additives in the NMP/C composite is clearly detected by Raman spectroscopy. Figure 3 represents the Raman spectra of carbon black additives before and after milling with NaMnPO$_4$. The Raman spectra are dominated by two intensive bands at 1326 and 1590 cm$^{-1}$. These two bands are defined as D (disorder) and G (graphite) peaks and they are fingerprints of disordered carbon with graphite-like medium-range order.[29-31] The G band is due to the in-plane stretching motion of pair of sp$^2$ carbon atoms in aromatic and olefinic bonding.[29-32] The D band is attributed to disorder-allowed phonon modes which become Raman active as a result of the disrupted symmetry of the graphite sheets (scattering from defects).[32] In the case of our samples, the positions of the D and G bands as well as their FWHM (full width at half maximum) values are not changed after the ball-milling process: 133/131 cm$^{-1}$ for the D bands and 78/82 cm$^{-1}$ for the G bands. On the other hand, the integrated intensity ratio $I_D/I_G$ (calculated by D- and G-band areas) shows a tendency to decrease after ball-milling of mixture of carbon black additives with

NaMnPO$_4$: 2.2 versus 1.8, respectively. The Raman spectroscopy gives evidence that the carbon is in a disordered state and this amorphous state is not modified by the ball-milling process. In addition, the amorphous state of carbon additives is consistent with the lack of XRD peaks due to carbon skeleton (Fig. 1).

In addition to the G and D bands, the Raman spectrum of NMP/C exhibits two low-intensity bands at 950 cm$^{-1}$ and at 648 cm$^{-1}$. These bands can be attributed to symmetric stretching and asymmetric bending modes ($\nu_1$ and $\nu_4$) of the PO$_4$ group. The $\nu_1$ band is much weaker than that in pristine NMP, which can be related to a screening effect of the carbon on the surface of the NaMnPO$_4$ particles.
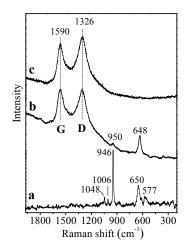


**Figure 3.** Raman spectra of NMP (a), NMP/C (b) and carbon additives (c).

The morphology of phospho-olivine is an important feature that determines their electrochemical properties. Figure 4 compares
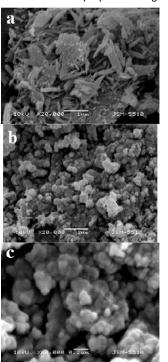


**Figure 4.** SEM images of pristine NMP (a) and NMP/C composite (b). For NMP/C, a higher magnification is used (c).

ARTICLE

the SEM images of NMP and NMP/C. The morphology of pristine NMP (Fig. 4 a) consists of rod-like aggregates with a length of about 0.5-1.0 μm and a width of about 0.10 – 0.15 μm. The ball-milling process, however, changes considerably the morphology of the composite NMP/C. It is visible that spherical aggregates instead of rod-like ones prevail in the SEM images (Fig. 4 b and c). This means that during the ball-milling the rods are being broken into small spherical aggregates with sizes below 100 nm (Fig. 4 c).

The TEM images show that NMP/C consists of well crystallized particles with sizes of about 50 nm (Fig. 5). Some of the particles are stacked into rod-like aggregates with smaller dimensions: i.e. 500/200 nm. As in the case of the SEM images, the rod-like aggregates appear to become smaller after ball-milling. The SAED pattern viewed along [013] reveals that nanoparticles are composed of single olivine-type of phase. The HRTEM image (Fig. 5) exhibits lattice fringes from (100) plane, the interplanar space of

1.05 nm coincides with that estimated by the XRD analysis (10.5156 Å). The TEM results confirm once again the stability of the olivine-type of structure during ball-milling procedure.

The important finding is that the olivine particles are covered with carbon additives; the coating thickness varies between 2 and 10 nm. In addition, some separate carbon particles with sizes of about 20 nm are also visible. The TEM investigation reveals that the ball-milling procedure followed by annealing at 400$^{\circ}$C is an effective way to ensure a good inter-phase contact between the olivine particles and the carbon additives.

The distributions of Na, Mn, P, O and C elements, determined using high angle annular dark field STEM images, are compared in Figure 5. It is clear that nano-particles have composition NaMnPO$_4$, which is homogeneously covered with carbon. The occurrence of separate individual carbon particles is also observed in the image of carbon element distribution.
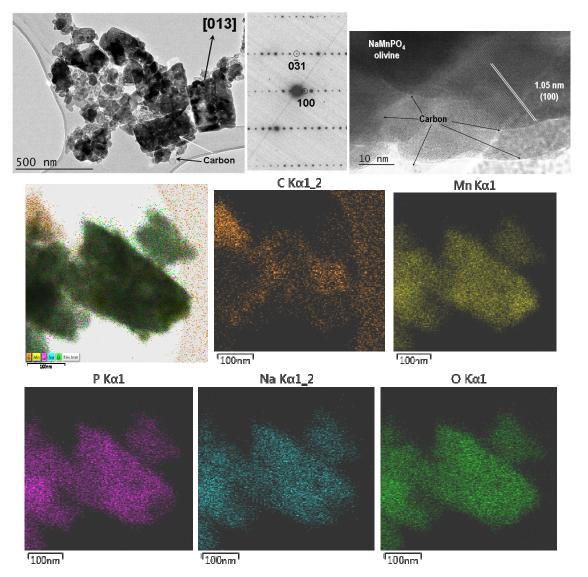


**Figure 5.** Bright field micrographs and SAED of composite NMP/C (left, first row); HRTEM image (right, first row); BF-STEM images and corresponding composition map of CK$\alpha_{1-2}$, MnK$\alpha_1$, PK$\alpha_1$, NaK$\alpha_{1-2}$ and OK$\alpha_1$.

### Chemical inertness of NaMnPO$_4$ phospho-olivine in the lithium electrolyte

Prior to the electrochemical tests it is necessary to understand the chemical innertness of NaMnPO$_4$ phase in the lithium electrolyte. It has been accepted that LiPF$_6$ is a highly reactive reagent due to its thermal instability.[33] LiPF$_6$ has been shown to decompose into LiF and PF$_5$ even at room temperature.[33] The reaction product PF$_5$ is a strong Lewis acid and it easily reacts with the surface of electrode materials leading to the formation of the solid-electrolyte inter-phase, containing a mixture of organic and inorganic compounds. Based on *ex-situ* micro-Raman spectroscopy, it has been found out that the delithiated Li$_x$MnPO$_4$ exhibits chemical instability in the LiPF$_6$-based electrolyte during a charge-discharge cycle, as a result of which pyrophosphate, Li$_4$P$_2$O$_7$ is being formed.[34] The degradation of LiMnPO$_4$ is significantly reduced when a phosphate surface is uniformly covered with carbon.[34] In addition, several chemical species, such as polycarbonates and carbonates, have been shown to be deposited on the surface of LiMnPO$_4$ during electrochemical cycling especially above 4.0 V vs. Li$^+$/Li.[35-37] Taking into account the possible interaction between phospho-olivines and lithium electrolyte, we studied the chemical reactivity of NaMnPO$_4$ with lithium electrolyte by soaking both NMP and NMP/C in the solution of LiPF$_6$ salt in EC/DMC solvent for 40 days. The soaked samples were then characterized by XRD and IR spectroscopic techniques.

Figure 6 compares the XRD patterns of pristine NMP and composite NMP/C before and after soaking them in the electrolyte. The XRD patterns of the soaked samples exhibit high level of background, but it is important that only diffraction peaks due to phospho-olivine phase become visible. Moreover, no shifts and changes in the intensities of the olivine diffraction peaks are observed. These characteristic features are valid for both the pristine and the carbon treated phospho-olivines. The constancy in the peak positions and intensities proves the chemical inertness of
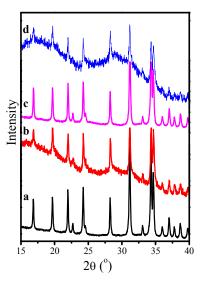
**Figure 6.** XRD patterns of: (a) pristine NMP; pristine NMP after soaking in the lithium electrolyte (b); NMP/C composite (c), and NMP/C after soaking in the electrolyte (d).

both pristine and carbon-treated NaMnPO$_4$ in the lithium electrolyte. This means that ion-exchange reactions of Na$^+$ from NaMnPO$_4$ for Li$^+$ from LiPF$_6$ salt are not taking place during the prolonged soaking.

The lack of side reactions is also confirmed by the IR spectra of the soaked samples. Since pristine and composite samples have one and the same behavior in the electrolyte, Figure 7 represents only the IR spectrum of NMP/C. To facilitate the assignment of IR bands, the same figure gives also the IR spectrum of fresh electrolyte (i.e. LiPF$_6$ solution in EC/DMC). The IR spectrum of soaked NMP/C is dominated by the vibrational bands due to LiPF$_6$, EC and DMC. In order to eliminate these bands, the soaked NMP/C sample is further washed with acetone. The comparison of IR spectra shows that only the bands due to the phosphate groups are resolved, their positions and intensities match well those of the pristine NMP/C. This observation gives evidence for the chemical inertness of NaMnPO$_4$ after storage in lithium electrolyte LiPF$_6$/EC/DMC. It is worth mentioning that no traces of pyrophosphates or polycarbonates, which are the usual products of side reactions, are
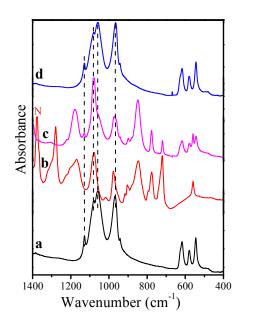
**Figure 7.** IR spectra of NMP/C composite (a), fresh electrolyte LiPF$_6$ in EC/DMC (b), NMP/C after soaking in the lithium electrolyte (c); NMP/C after soaking in the lithium electrolyte and washed with acetone (d). "N" denotes the band from Nujol oil.

detected by IR spectroscopy.

### Electrochemical properties of composites NaMnPO$_4$/C

Figure 8 compares the first charge/discharge curves of NaMnPO$_4$. For the sake of comparison, the same figure gives also the charge/discharge curve of LiMnPO$_4$ analogue covered with carbon following the same treatment procedure. All cells start with a charging mode, where Li$^+$ and Na$^+$ deintercalation from phospho-olivines is expected to occur. For LiMnPO$_4$, the main oxidation and reduction peaks corresponding to the Mn$^{2+}$/Mn$^{3+}$ redox couple

appear at 4.3 and 3.9 V, respectively. The capacity delivered during the first charging and consecutive discharging reaches 165 and 150 mAh/g. These values are close to the theoretical one (i.e. 168 mAh/g), which indicates a lack of polarization for the cell based on LiMnPO$_4$ electrode. The good electrochemical performance can be related to a close contact between carbon additives and LiMnPO$_4$. It is well known that carbon additives play a crucial role in improving the electrochemical performance of LiMnPO$_4$: on the one hand, the carbon additives have a positive impact on the electrical conductivity and chemical stability of phospho-olivines and, on the other hand, they ensure a good wetting of NaMnPO$_4$ with electrolyte solution. The electrochemical performance of LiMnPO$_4$, used by us as a reference, points out that ball-milling procedure followed by thermal treatment at 500 $^o$C is a successful method to overcome the drawbacks typical of LiMnPO$_4$-based electrode material.

In comparison with LiMnPO$_4$, its sodium analogue NaMnPO$_4$ delivered a capacity that is slightly lower. During the first charging, the potential corresponding to the Na$^+$ ion deintercalation depends on the charging rate: at a slow rate, the potential tends to that typical of Mn$^{2+}$/Mn$^{3+}$ in the LiMnPO$_4$ analogue. On the contrary, the reverse discharging process is proceeding at lower potential than that for LiMnPO$_4$: 3.75 versus 3.95 V. It is worth mentioning that the discharging rate does not affect the discharge potential. This allows assigning the two plateaus at 4.25 (charge) and 3.75 V (discharge) to the Mn$^{2+}$/Mn$^{3+}$ couple too. The stability of capacity during cycling is shown in Figure 8. After the first three cycles, both charge and discharge capacities become close during cycling, the Columbic efficiency being more than 98 %. The reversible capacity reaches 80-85 mAh/g, which corresponds to 0.5 mol of intercalated alkaline
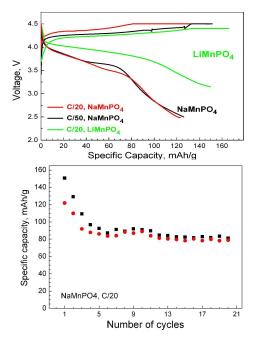




**Figure 8.** First charging/discharging curves for NaMnPO$_4$ and LiMnPO$_4$ used as electrodes in model lithium cells. The charge and discharge capacity (black and red symbols) for NaMnPO$_4$ versus the number of cycles.

ions. These results are the first experimental evidence that NaMnPO$_4$ is electrochemically active in the model lithium cell.

As a support of the electrochemical activity of NaMnPO4 in a lithium cell, Figure 9 gives the CV curve of NaMnPO$_4$/C in a broad potential range from 1.7 to 4.7 V. The CV curve displays one well-resolved peak at 4.38 V in the anodic scan and two peaks at 3.94 and 3.10 V in the cathodic scan. Below 2.5 V, additional less intensive peaks are resolved. Above 4.5 V, the strong increase in the current implies for a possible electrode-electrolyte interaction. Taking into account the CV data, the galvanostatic cycling was limited between 2.5 and 4.5 V. The anodic and cathodic peaks at 4.38 and 3.94 V coincide with that typical for LiMnPO$_4$: for carbon-coated LiMnPO$_4$ with a particle size of 30-70 nm the cathodic and anodic peaks are at 4.093 and 4.307 V, respectively, while for LiMnPO$_4$ with a bigger particle size the peaks are at 3.930 and 4.544 V, respectively. [38] In our case of carbon coated NaMnPO$_4$ with a particle size below 100 nm the peak positions are between above limiting cases of LiMnPO$_4$. This result reveals unambiguously that lithium intercalation takes place into NaMnPO$_4$ thanks to the oxidation and reduction of manganese ions (i.e. Mn$^{2+}$/Mn$^{3+}$ ionic pair). However, the cathodic peak at 3.10 V is not associated with lithium intercalation. Thus, the main question is: what is the origin of the intercalation reaction of NaMnPO$_4$ in a lithium cell?
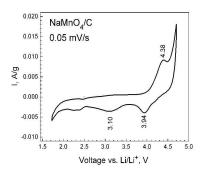


**Figure 9.** CV curve of NaMnPO4/C in a lithium cell after 5 galvanostatic cycles between 2.5 and 4.5 V.

In order to understand the nature of the electrochemical activity of NaMnPO$_4$ in lithium cells, ex-situ XRD, IR, TEM and EPR experiments have been undertaken. Fig. 10 represents the *ex-situ* XRD pattern of an electrode NMP/C after 5 cycles between 4.5 and 2.5V at C/50. (The cell is stopped at 2.5 V.) For comparison, the XRD pattern of an electrode NMP/C prior to the electrochemical cycling is also given. The non-cycled electrode displays the well-resolved diffraction peaks corresponding to the olivine phase only (Fig. 10 a,c). After 5 cycles, the background level increases significantly, but the relatively weak diffraction peaks due to olivine phase are still well resolved (Fig. 10b). On the basis of (200), (210), (020), (301), (311) and (121) diffraction peaks, it is possible to estimate the lattice parameters: $a$ = 10.452 Å, $b$ = 6.266 Å, $c$= 4.994 Å, $V$ = 327.06 Å$^3$. The estimated lattice parameters are slightly lower than those of pristine NaMnPO$_4$ ($a$ = 10.5177(3) Å, $b$ = 6.3144(2) Å, $c$= 4.9873(2) Å, $V$ = 331.227(22) Å$^3$), but they are higher in comparison to the lithium ones LiMnPO$_4$ obtained by ion-exchange reaction [22] ($a$ =10.488(1) Å, $b$ = 6.1006(8) Å, $c$= 4.7518(8) Å, $V$ =302.901 Å$^3$). The

comparison indicates that phospho-olivine phase with sodium content slightly lower than 1 mol participates in a reversible intercalation/deintercalation cycling when $NaMnPO_4$ is used as a cathode in model lithium cell. This means that $Na^+$ intercalation proceeds together with $Li^+$ intercalation during the lithium cell discharging. The occurrence of sodium-rich phospho-olivine phase in discharged lithium cell is an opposite behavior compared to that of sodium transition metal oxides with a layered structure $Na_xNi_{0.5}Mn_{0.5}O_2$.[12] We have demonstrated that $Li^+$ intercalation proceeds easily in $Na_xNi_{0.5}Mn_{0.5}O_2$ during lithium cell discharging, as a result of which mixed lithium-sodium oxides with Li-to-Na ratio higher than 6 are being formed.[12]
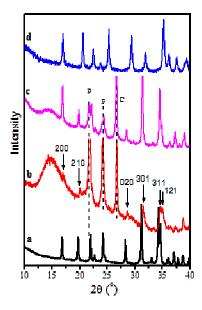


**Figure 10.** XRD patterns of NMP/C composite (a), NMP/C after 5 charge-discharge cycles between 4.5 and 2.5V at C/50 (b), NMP/C electrode prior to cycling (c) and $LiMnPO_4$ (d). Symbols "P" and "C" denote the diffraction peaks due to parafilm and graphite.

The TEM analysis allows gaining insight into the structure stability of phospho-olivines during cell operation (Fig. 11). After the intercalation/deintercalation cycling, the morphology of NMP/C is preserved. There are well-crystallized particles with dimensions close to those before the cycling experiment. In addition, the rod-like aggregates are also distinguishable in the TEM image of cycled electrode. The lattice parameters determined by SAED are comparative with those of $NaMnPO_4$. Taking into account the accuracy in the determination of lattice parameters by TEM (less than 1.5 %), it is not possible to detect precisely the small deviations of the lattice parameters as it was observed by XRD experiments. However, HRTEM reveals that the degree of crystallinity of phospho-olivine phase is also preserved after the intercalation/deintercalation cycling.

The distributions of Na, Mn, P and O elements in particles with nanometric dimensions are given in Figure 11. In these particles, all

Na, Mn, P and O are homogeneously distributed. It is worth mentioning that, in addition to Na, Mn, P and O, the peak due to F element is also resolved (not shown). This indicates presence of electrolyte on the NMP/C electrode surface. The important finding from STEM is related with the ratio of Na-to-Mn. The Na-to-Mn ratio in NMP/C is 1.04, which matches well with the chemical composition of phospho-olivine $NaMnPO_4$. After the intercalation/deintercalation cycling, there is a decrease in the Na-to-Mn ratio, which varies for the different particles from 0.55 to 0.75. This decrease in the sodium content is in agreement with XRD data, according to which the phospho-olivine phase has a slightly shrunk unit cell. Combining the results from TEM and XRD analysis of the cycled electrodes, it appears that the olivine-phase participates in the reversible intercalation/deintercalation cycling without changing its structure and degree of crystallinity, accompanied by a loss of Na of about 25 - 45%.

The IR spectroscopy gives evidence for lithium intercalation in $NaMnPO_4$. Figure 12 compares the IR spectra of two electrode compositions: NMP/C before the cycling experiment and NMP/C after 5 cycles between 2.5 and 4.5 V. The IR spectra of its $LiMnPO_4$ analogue, PVDF and lithium electrolyte are also shown. Two specific features can be distinguished. First, the comparative analysis shows that the IR spectra of electrode compositions before and after cycling are identical in the range, where $PO_4$ vibrations appear. It is noticeable that, in this range, the IR spectra of both sodium and lithium phospho-olivines are also quite close (especially with respect to band positions). Second, the IR spectra of $NaMnPO_4$ and $LiMnPO_4$ analogues can be clearly distinguished in the range 450 – 490 $cm^{-1}$, where Li-O translations appear. Close inspection of the IR spectrum of NMP/C after the intercalation/deintercalation cycling indicates the appearance of two weak bands at 496 and 453 $cm^{-1}$, which have not been detected with NMP/C before the cycling. These bands coincide with those typical of Li-O translations observed for $LiMnPO_4$. It should be taken into account that in this IR range both electrolyte and PVDF compound do not show any strong IR bands. Therefore, the two weak bands at 496 and 453 $cm^{-1}$ are attributed to Li-O translations. The appearance of these bands in the IR spectrum of cycled electrode is a spectroscopic evidence for the intercalation of $Li^+$ in $NaMnPO_4$ after the cycling. The spectroscopic evidence is in a good agreement with CV data, where the lithium intercalation takes place at 4.38 and 3.94 V (Fig. 9). This allows attributing the second cathodic peak at 3.10 V to sodium intercalation reaction into $Na_xMnPO_4$ (Fig. 9). It is worth mentioning that Li+ and Na+ intercalation proceeds at two separate potentials, while their deintercalation processes are not distinguished in the anodic scan of the CV curve (Fig. 9). This is an interesting result, which deserves further investigation. Combining TEM, IR spectroscopic and CV data, the most probable chemical reaction is the reversible exchange of 0.5 mol of alkali ions between $Li_{(0.25-0.45)}Na_{(0.75-0.55)}MnPO_4 \leftrightarrow Li_{0.0}Na_{0.5}MnPO_4$. The formation of mixed lithium-sodium manganese phospho-olivine in discharged state is an unexpected result, which can serve as guidance to design novel polyanion-based electrode materials.
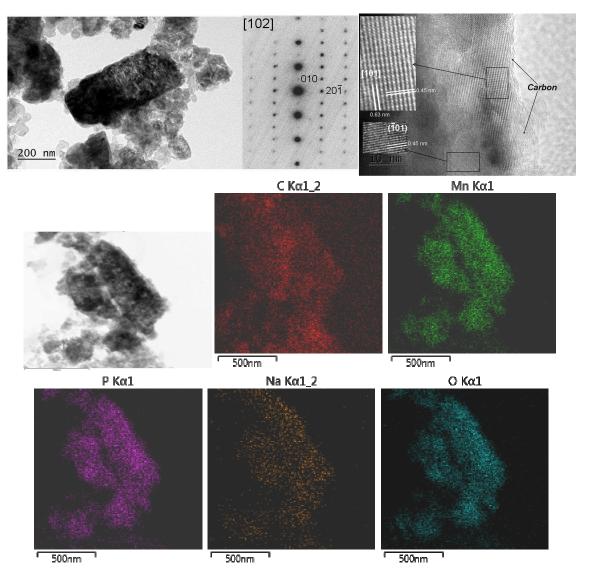
**Figure 11.** *ex-situ* Bright field micrographs and SAED of NMP/C electrode cycled 5 times between 2.5 and 4.5 V at C/50 in a model lithium cell (left, first row); HRTEM image (right, first row); BF-STEM images and corresponding composition map of $CK\alpha_{1-2}$, $MnK\alpha_1$, $PK\alpha_1$, $NaK\alpha_{1-2}$ and $OK\alpha_1$.

To elucidate the nature of the electrochemical activity of $NaMnPO_4$, we used EPR spectroscopy in order to monitor the changes in the oxidation state of manganese ions. Figure 13 gives the EPR spectra of NMP/C electrodes before and after the cycling experiments. The EPR spectrum of non-cycled NMP/C consists of a single Lorentzian line. The *g*-factor is constant in the temperature range of 100-300 K, whereas the EPR line width ($\Delta H_{pp}$) increases considerably upon cooling (Fig. 14). The temperature dependence of the EPR signal intensity obeys the Currie-Weiss law between 180 and 300 K, where Weiss constant is - 118 ± 6 K. These parameters can be assigned to $Mn^{2+}$ ions coupled by strong exchange interactions. It is worth mentioning that the magnetic structure of $NaMnPO_4$ has not been studied yet. However, we can compare the EPR data of $NaMnPO_4$ with those for $LiMnPO_4$ analogue, whose magnetic structure is well documented. $LiMnPO_4$ displays

antiferromagnetic long-range order below 34 K. The magnetic structure of $LiMnPO_4$ includes in-plane super-exchange interactions between the $Mn^{2+}$ ions via oxygen (*bc*-plane) and interlayer coupling through the phosphate groups along the [100] direction.[39] The magnetic interactions between $Mn^{2+}$ are responsible for the appearance of a single Lorentzian line in the EPR spectrum of $LiMnPO_4$ at temperatures above that of the magnetic order.[40-42] The comparison between EPR spectra of both sodium and lithium phases shows that their parameters are quite similar: *g*=2.004 and $\Delta H_{pp}$=20 mT for $NaMnPO_4$ in comparison with g=1.99 and $\Delta H_{pp}$=18 mT for $LiMnPO_4$ [22]. This fact confirms that exchange-coupled $Mn^{2+}$ ions contribute to the origin of the EPR spectrum of $NaMnPO_4$. In addition, the EPR parameters of $NaMnPO_4$ in the fabricated electrode NMP/C before cycling and in the composite $NaMnPO_4$/C in the form of powder are close (Fig. 14).
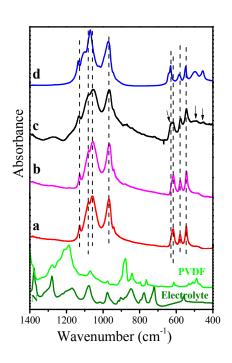
**Figure 12.** IR spectra of NMP/C composite (a), NMP/C electrode prior to electrochemical reaction (b), NMP/C electrode after 5 charging-discharging cycles between 4.5 and 2.5V at C/50 (c), LiMnPO$_4$ reference (d). For the sake of comparison, PVDF and electrolyte LiPF$_6$/EC/DMC are also given.

After the cycling, the EPR spectrum undergoes a strong change. There are two overlapping signals (Fig. 13). The first signal (Si1) has a *g*-factor and line width similar to those before the cycling (Fig. 14). The Weiss constant value, determined from the temperature dependence of the signal intensity, is also similar: -134 ± 19  K. The similar EPR parameters reveal unambiguously that the first signal originates from the Mn$^{2+}$ ions, localized in the unreacted NaMnPO$_4$
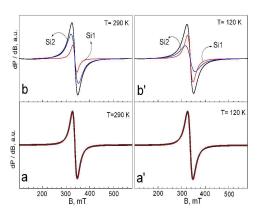


**Figure 13.** EPR spectra at 290 and 120 K of NMP/C electrode before the electrochemical reaction (a, a'); NMP/C electrode after 5 cycles between 2.5 and 4.5 V (b, b'). The black curves are the experimental EPR spectra, while the red and blue curves correspond to the deconvoluted signal 1 and signal 2.

phase.  The second signal (Si2) is broader and it possesses higher g-factor in comparison with that of the first signal. In addition, both the g-factor and the line width increase upon cooling down. Although the *g*-value of Si2 falls within the typical range for Mn$^{2+}$ ions, the temperature dependence of the g-factor reveals that the second signal is due to a complex spin system rather than to exchange-coupled Mn$^{2+}$ ions. This can be explained, if we suppose that highly oxidized Mn ions appear together with Mn$^{2+}$ ions and all these manganese ions contribute to the second broad signal. Taking into account the charging-discharging curves (Fig. 8a), the redox couple Mn$^{2+}$/Mn$^{3+}$ is responsible for the alkaline ion intercalation in the phospho-olivine matrix. In contrast to Mn$^{2+}$ ions, the Mn$^{3+}$ ions are unlikely to be detectable by EPR in the X-band region (i.e. at 9.4 GHz) due to their strong spin-lattice relaxation and large zero-field splitting parameters. However, their effect on the EPR response of Mn$^{2+}$ ions is easily observable. The same picture has been observed for several layered and spinel oxides (such as lithium manganese spinels, delithiated lithium nickel manganese oxides, sodium deficient manganese oxides), where Mn$^{3+}$ and Mn$^{4+}$ coexist.[9,43] (It should be reminded that both Mn$^{2+}$ and Mn$^{4+}$ are to be observed easily by X-band EPR even at room temperature.) Therefore, the second signal is assigned to Mn$^{2+}$ ions, whose parameters are perturbed by Mn$^{3+}$ ions. This is consistent with the temperature dependence of the signal intensity: between 200 and 300 K, the signal intensity is changing following the Curie-Weiss law with a Weiss constant of -365 K. On the one hand; the EPR signal is related to irreversibility of the electrochemical reaction, as a result of which Mn$^{3+}$ ions appear in addition to Mn$^{2+}$ ones. On the other hand, this is a direct spectroscopic evidence for oxidation and reduction of manganese ions during the intercalation/deintercalation cycling.
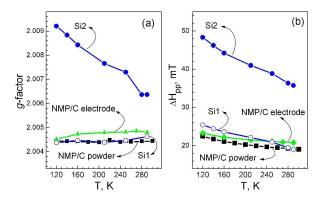


**Figure 14.** Temperature dependence of the g-factor (b) and EPR line width (b) for NMP/C powder (square symbols), NMP/C electrode before the electrochemical reaction (triangular symbols) and NMP/C electrode after 5 cycles between 2.5 and 4.5 V at C/50 (open and full circles for Si1 and Si2).

## Conclusions

Composite materials NaMnPO$_4$/C are obtained by ball-milling of pristine NaMnPO$_4$ with conductive carbon black additives Super C/65. The ball-milling leads to a fragmentation of the

　　　　　　　　　　　　　　　　　　　　　　　　　　　　　　　　　　　**ARTICLE**

rod-like aggregates of $NaMnPO_4$ into smaller species, accompanied by their dense covering with carbonaceous materials. The covering layer thickness varies between 2 and 10 nm. The carbonaceous skeleton is composed of disordered carbon structure with graphite-like medium-range order, which remains intact during ball-milling process. The phospho-olivine structure is also stable in regard to mechanical milling.

The composite $NaMnPO_4$/C material displays relatively good electrochemical activity, when used as a cathode in model lithium ion cells. Prior to the electrochemical test, the composite $NaMnPO_4$/C does not react with the lithium electrolyte containing 1M $LiPF_6$ solution in ethylene carbonate and in dimethyl carbonate. During the first charging, almost all of $Na^+$ ions are being extracted from $NaMnPO_4$ at voltage plateau of 4.25 V, which coincides well with that typical of $LiMnPO_4$ analogue. During the consecutive discharging, there is a competition between $Li^+$ and $Na^+$ intercalation into $NaMnPO_4$, which is manifested by a sloping galvanostatic voltage curve. The CV curves reveal that $Li^+$ and $Na^+$ intercalation proceeds at two separate potentials, while their deintercalation processes are not distinguished in the anodic scan. The reversible intercalation/deintercalation cycling proceeds with an exchange of 0.5 mol alkaline ions, the most probable chemical reaction being $Li_{(0.25-0.45)}Na_{(0.75-0.55)}MnPO_4 \leftrightarrow Li_{0.0}Na_{0.5}MnPO_4$. The reversible intercalation of $Li^+$ and $Na^+$ takes place owing to the redox $Mn^{2+}/Mn^{3+}$ couple.

As far as we know, the reversible $Li^+$ and $Na^+$ intercalation into sodium manganese phospho-olivines is reported experimentally for the first time. The electrochemical performance of $NaMnPO_4$ in lithium ion cells is not yet competitive compared to the well-known $LiMnPO_4$ analogue. However, by optimizing the electrolyte solutions, it would be possible to stimulate the single ion intercalation instead of double ion intercalation. By both facilitating lithium intercalation and depressing sodium intercalation, one can expect to transform $NaMnPO_4$ into $LiMnPO_4$ during the first cycles. Thus, the *in-situ* generated $LiMnPO_4$ will further operate and, most probably, it will be characterized with improved electrochemical performance in comparison with conventional $LiMnPO_4$ due to size-dependent effects. In this context, these first studies demonstrate clearly a significance of the sodium manganese phospho-olivine as an electrode material in alkaline ion batteries.

## Acknowledgements

## References

1　Z. Gong and Yong Yang, *Energy Environ. Sci.*, 2011, **4**, 3223.

2　C. Masquelier and L. Croguennec, *Chem. Rev.,* 2013, **113**, 6552.

3　D. Choi, D. Wang, I.-T. Bae, J. Xiao, Z. Nie, W. Wang, V.V. Viswanathan, Y.J. Lee, J.-G. Zhang, G.L. Graff, Z. Yang and J. Liu, *Nano Lett.* 2010, **10**, 2799.

4　C. Delacourt, L. Laffont, R. Bouchet, C. Wurm, J.-B. Leriche, M. Morcrette, J.-M. Tarascon and C.J. Masquelier, *J. Electrochem. Soc.* 2005, **152**, A913.

5　A. Morgan, A. Van der Ven, G. Ceder, *Electrochem. Solid-State Lett.* 2004, **7**, A30.

6　Wang, X. Sun, *Energy Environ. Sci.*, 2012, **5**, 5163.

7　L. Dimesso, C. Förster, W. Jaegermann, J. P. Khanderi, H. Tempel, A. Popp, J. Engstler, J. J. Schneider, A. Sarapulova, D. Mikhailova, L. A. Schmitt, S. Oswald and H. Ehrenberg, *Chem. Soc. Rev.*, 2012, **41**, 5068.

8　C. Delacourt, P. Poizot, M. Morcrette and J.-M. Tarascon and C. Masquelier, *Chem. Mater.*, 2004, **16**, 93.

9　M. Yoncheva, R. Stoyanova, E. Zhecheva, E. Kuzmanova, M. Sendova-Vassileva, D. Nihtianova, D. Carlier, M. Guignard and C. Delmas, *J. Mater. Chem.* 2013, **22**, 23418.

10　M. Kalapsazova, R. Stoyanova and E. Zhecheva, *J. Solid State Electrochem.,* 2014, **18**, 2343.

11　M. Kalapsazova, R. Stoyanova, E. Zhecheva, G. Tyuliev and D. Nihtianova, *J. Mater. Chem. A,* **2014**, 2, 19383.

12　M. Kalapsazova, G.F. Ortiz, J.L. Tirado, O. Dolotko, E. Zhecheva, D. Nihtianova, L. Mihaylov and R. Stoyanova, *ChemPlusChem* DOI: 10.1002/cplu.201500215.

13　Y. Tang, D. Sun, H. Wang, X. Huang, H. Zhang, S. Liu and Y. Liu, *RSC Adv.* 2014, **4**, 8328-8334.

14　H. Wang, S. Liu, Y. Ren, W. Wang and A. Tang, *Energy Environ. Sci.,* 2012, **5**, 6173.

15　S. Bach, J.P. Pereira-Ramos and P. Willmann, *Electrochim. Acta,* 2006, **52**, 504.

16　M. Shirpour, J. Cabana and M. Doeff, *Energy Environ. Sci.* 2013, **6**, 2538.

17　M. Gnanavel, V. Pralong, O. I. Lebedev, V. Caignaert, P. Bazin and B. Raveau, *Chem. Mater.* 2014, **26**, 4521.

18　P. B. Moore, *Am. Mineral.*, 1972, **57**, 1333.

19　J. Moring and E. Kostiner, *J. Solid State Chem.*, 1986, **61**, 379.

20　C. A. J. Fisher and M. Saiful Islam, *J. Mater. Chem.*, 2008, **18**, 1209.

21　S. P. Ong, V. L. Chevrier, G. Hautier, A. Jain, C. Moore, S. Kim, X.Ma and G. Ceder, *Energy Environ. Sci.*, 2011, **4**, 3680.

22　V. Koleva, E. Zhecheva and R. Stoyanova, *Dalton Transactions*, 2011, **40**, 7385.

23　V. Koleva, T. Boyadzhieva, E. Zhecheva, D. Nihtianova, S. Simova, G. Tyuliev and R. Stoyanova, *CrystEngComm,* 2013, **15**, 9080.

24　V. Koleva, R. Stoyanova, E. Zhecheva and D. Nihtianova, *CrystEngComm* 2014, **16**, 7515.

25　J. Rodrıguez-Carvajal, *Commission on Powder Diffraction Newsletter* 2001, **26**, 12.

26　J. Rodriguez-Carvajal, Abstracts of the Satellite Meeting on Powder Diffraction of the XV Congress of the IUCr, Toulouse, 1990.

27　H. Fang, Z. Pan, L. Li, Y. Yang, G. Yan, G. Li and S. Wei, *Electrochem. Commun.* 2008, **10**, 1071.

28　K. T. Lee, T. N. Ramesh, F. Nan, G. Botton and L. F. Nazar, *Chem. Mater.*, 2011, **23**, 3593.

29　Y. Liu, C. Pan, J. Wang, *J. Mater. Sci.,* 2004, **39**, 1091.

30　F. Tuinstra and J.L. Koenig, *J. Chem. Phys.*, 1970, **53**, 1126.

31　J. Robertson, *J Non Cryst Solids,* 2002, **299–302**, 798.

32　A.C. Ferrari and J. Robertson, *Phys. Rev. B*, 2000, **61**, 14095.

33　K. Xu, *Chem. Rev.*, 2004, **104**, 4303.

34　N.S. Norberg and R. Kostecki, *J. Electrochem. Soc.* 2012, *159*, A1431.

35　K. Edström, T. Gustafsson and J.O. Thomas, *Electrochim. Acta*, 2004, **50**, 397.

36  J. W. Lee, M. S. Park, B. Anass, J. H. Park, M. S. Paik and S. G. Doo, *Electrochim. Acta*, 2010, **55**, 4162.

37  D. Choi, J. Xiao, Y.J. Choi, J.S. Hardy, M. Vijayakumar, M. S. Bhuvaneswari, Jun Liu, W. Xu, W. Wang, Z. Yang, G.L. Graff and J.-G. Zhang, *Energy Environ. Sci.*, 2011, **4**, 4560.

38  K. Wang, Y. Wang, C. Wang and Y. Xia, *Electrochim. Acta* 2014, **146,** 8.

39  J. Li, W. Tian, Y. Chen, J. L. Zarestky, J. W. Lynn and D. Vaknin, *Phys. Rev. B: Condens. Matter Mater. Phys.*, 2009, **79**, 144410.

40  D. Arčon, A. Zorko, P. Cevc, R. Dominko, M. Bele, J. Jamnik, Z. Jagličić and I. Golosovsky, *J. Phys. Chem. Solids*, 2004, **65**, 1773.

41  N. Wizent, G. Behr, F. Lipps, I. Hellmann, R. Klingeler, V. Kataev, W. Löser, N. Sato and B. Büchner, *J. Cryst. Growth*, 2009, **311**, 1273.

42  D. Arčon, A. Zorko, R. Dominko and Z. Jagličić, *J. Phys.: Condens. Matter*, 2004, **16**, 5531

43  (a) R. Stoyanova,  E. Zhecheva and S. Vassilev, *J. Solid State Chem.*, 2006, **179**, 378; (b) R. Stoyanova, D. Carlier, M. Sendova-Vassileva, M. Yoncheva, E. Zhecheva, D. Nihtianova, C. Delmas, *J. Solid State Chem.,* 2010*,* **183**, 1372; (c) R. Stoyanova,  E. Zhecheva, R. Alcántara and J.L. Tirado, *J. Mater. Chem.*, 2006, **16**, 359; (d) E. Zhecheva, R. Stoyanova, R. Alcántara, P. Lavela, J.L. Tirado, *J. Power Sources,* 2007, **174**, 519.